

Uncovering hydrogen anion triggered thermal runaway mechanism of a high-energy $\text{LiNi}_{0.5}\text{Co}_{0.2}\text{Mn}_{0.3}\text{O}_2$ /graphite pouch cell

Lang Huang

Qingdao Institute of Bioenergy and Bioprocess Technology, Chinese Academy of Sciences

Gaojie Xu

Qingdao Industrial Energy Storage Research Institute, Qingdao Institute of Bioenergy and Bioprocess Technology, Chinese Academy of Sciences

Xiaofan Du

Qingdao Institute of Bioenergy and Bioprocess Technology

Jiedong Li

Qingdao Institute of Bioenergy and Bioprocess Technology, Chinese Academy of Sciences

Bin Xie

Qingdao Institute of Bioenergy and Bioprocess Technology, Chinese Academy of Sciences

Di Lu

Qingdao Industrial Energy Storage Research Institute, Qingdao Institute of Bioenergy and Bioprocess Technology, Chinese Academy of Sciences

Haisheng Liu

Qingdao Industrial Energy Storage Research Institute, Qingdao Institute of Bioenergy and Bioprocess Technology, Chinese Academy of Sciences

Min Zhao

Qingdao Institute of Bioenergy and Bioprocess Technology, Chinese Academy of Sciences

Pengxian Han

Chinese Academy of Sciences

Shanmu Dong

Qingdao Institute of Bioenergy and Bioprocess Technology

Guanglei Cui (✉ cuiql@qibebt.ac.cn)

Qingdao Institute of Bioenergy and Bioprocess Technology, Chinese Academy of Sciences
<https://orcid.org/0000-0001-5987-7569>

Liquan Chen

Institute of Physics

Keywords: lithium ion batteries, thermal runaway route map depiction, thermal runaway prevention

Posted Date: January 8th, 2021

DOI: <https://doi.org/10.21203/rs.3.rs-132558/v1>

License:  This work is licensed under a Creative Commons Attribution 4.0 International License.

[Read Full License](#)

Abstract

The continuous energy density increase of lithium ion batteries (LIBs) inevitably accompanies with the rising of safety concerns. Here, the thermal characteristics of a high-energy 5 Ah $\text{LiNi}_{0.5}\text{Co}_{0.2}\text{Mn}_{0.3}\text{O}_2$ /graphite pouch cell using a thermally stable dual-salt electrolyte were analyzed. Heat determination during cycling at two boundary scenarios of adiabatic and isothermal environment clearly states the necessity of designing an efficient and smart battery thermal management system. More importantly, it is innovatively proposed that the hydrogen anion (H^-) induced H_2 releasing at anode side and H_2 migration to cathode side is the rooted thermal runaway trigger of the pouch cell, while the phase transformation of lithiated graphite anode and the O_2 -releasing by delithiated cathode are just accelerating factors for thermal runaway. These findings will shed promising lights on thermal runaway route map depiction and thermal runaway prevention, as well as formulation of electrolyte for high energy safer LIBs.

Introduction

This decade has witnessed the increasing challenges coming from petrochemical energy crisis and environmental pollution. Hence, the demand for developing advanced and renewable energy technology with clean processes and high efficiency is becoming more and more necessary. Great efforts towards promoting alternative renewable energy resources (such as solar, wind, photovoltaic and tidal energy, *etc.*) have been devoted.¹ The intermittent nature of these renewable energy resources facilitates the booming of varied energy storage systems. Due to their advantages like high energy density, low maintenance and longevity, the promising energy storage system of Li-ion batteries (LIBs) have been widely used in varied fields ranging from small portable electronics to large-scale electric vehicles.²⁻³

Recently, the on-going “endurance mileage” anxiety has stimulated the energy density increase of LIBs, and great efforts has been made on understanding the inherent electrochemistry as well as developing advanced material systems. However, the energy density increase of LIBs inevitably accompanies the rising of safety concerns.⁴⁻⁷ Compulsory and strict testing standards are applied for LIBs before their entrance into market, and the thermal characteristics research of LIBs is kept attracting widely attentions. At present, varied testing approaches, such as accelerating rate calorimetry (ARC),⁸⁻¹² differential scanning calorimetry (DSC),¹³⁻¹⁵ C80 micro-calorimeter,¹⁶⁻¹⁷ and isothermal microcalorimetry (IMC),¹⁸⁻²⁰ *etc.*, have been employed to investigate thermal characteristics and thermal runaway mechanism of LIBs. Conventionally, the thermal runaway mechanism of LIBs is demonstrated to be associated with a series of exothermic chain reactions, including decomposition of solid electrolyte interface (SEI) layer, anode/electrolyte reactions, self-decomposition of electrolyte, and cathode/electrolyte reactions, *etc.*²¹⁻²⁵ However, very recently, Prof. M. Ouyang *et al.* revealed that the oxygen released from nickel-manganese-cobalt (NMC) cathode will be consumed by the lithiated anode with great heat generation, triggering the thermal runaway of LIBs.¹⁰ Differently, by analyzing the released gas, N. E. Galushkin *et al.* propose that the powerful exothermic reaction from recombination of atomic hydrogen accumulated at anode graphite

will contribute to the initiation of thermal runaway of LIBs.²⁶ It is noted here that, battery thermal runaway will occur at any state of charge (SOC) in practical cases. But in most of previous reports, the thermal runaway mechanisms are always deciphered at high SOC. Until now, due to the complexity of exothermic chain reactions inside LIBs and the limitation of the existing testing approaches for thermal safety study, it is still difficult to obtain a clear and accurate thermal runaway route map depicting the rooted interactions among cathode, anode, electrolyte and separator.

Obviously, during the hazardous thermal runaway (smoke, fire and even explosion) of LIBs, electrolyte is almost involved in every exothermic chain reaction.^{4, 27-28} As the “blood” of the LIBs, the organic electrolyte has a crucial influence on the electrochemical and inherent thermal safety of LIBs. Lithium hexafluorophosphate (LiPF₆) with well-balanced properties is always adopted as the main conducting lithium salt for the widely commercialized carbonate-based electrolytes. However, the thermally unstable and moisture sensitive LiPF₆ is susceptible to generate undesired reactive species such as HF and POF₃, inducing the destruction of electrode/electrolyte interface layers and the transition metals dissolution from cathode.²⁹⁻³¹ Hence, tremendous efforts have been devoted to design and synthesize alternative lithium salts.^{29, 32} Wherein, thermally stable and highly conductive lithium imides of lithium bis(trifluoromethanesulfonyl) imide (LiTFSI) and lithium bis(fluorosulfonyl) imide (LiFSI) have aroused great interests. But, both LiTFSI and LiFSI easily cause corrosion of Al current collector at high voltages exceeding 4 V.³³⁻³⁶ Formulating high cost concentrated electrolyte will effectively prohibit LiFSI-induced Al corrosion, but, the LIB still undergoes thermal runaway due to the strong heat-releasing reaction between LiFSI salt and lithiated graphite.²³ Another economic way to suppress Al corrosion is to formulate blended-salt electrolytes by mixing LiTFSI or LiFSI with lithium difluoro(oxalate) borate (LiDFOB) or lithium bis(oxalato)borate (LiBOB).^{9, 28, 36-43} Recently, blended-salt electrolytes showing synergistic effects have achieved great progress in the burgeoning field of next-generation lithium batteries.²⁸ Nevertheless, to the best of our knowledge, the electrochemical and thermal safety evaluation of blended-salt electrolytes in large format and large capacity LIBs are seldom reported.

Here, we conduct electrochemical and thermal safety study of a pouch-type 5 Ah LiNi_{0.5}Co_{0.2}Mn_{0.3}O₂/graphite (NCM523/G) battery with a dual-salt electrolyte, which is formulated by dissolving LiTFSI and LiDFOB lithium salts in carbonate solvents of ethylene carbonate (EC), propylene carbonate (PC), and ethyl methyl carbonate (EMC). In specific, the electrochemical performances of 5 Ah NCM523/G pouch cell are investigated over a wide temperature range (-40°C ~ 60°C). To state the importance of designing an efficient and smart battery thermal management system, heat generation of 5 Ah NCM523/G pouch cell during charge-discharge processes is determined at both adiabatic (ARC) and isothermal (IMC) conditions. More importantly, varied advanced characterization techniques (such as temperature-resolved XRD, ARC, *on-line* titration gas analysis system) are used to elucidate the thermal compatibility of battery materials disassembled from pouch cell with different SOC (100% and 0%). Finally, we innovatively propose that the hydrogen anion (H⁻) induced H₂ releasing at anode side and H₂ migration to cathode side is the rooted thermal runaway trigger of this NCM523/G pouch cell, while the

phase transformation of lithiated graphite anode and the O₂-releasing by delithiated NCM523 cathode are just accelerating factors for thermal runaway. This study provides a deeper insight for understanding of the inherent mechanism of thermal runaway of LIBs, and lights the way to advanced design philosophy of next generation safer LIBs.

Results And Discussion

Electrochemical performances over a wide temperature range

Undoubtedly, LIBs operating over a wide temperature range presents great importance in practical applications such as those in electric vehicles, space and military missions. For wide temperature LIBs, the most challenging work is to get a compromise between subzero temperature performance and high temperature performance. The most direct and efficient strategy is formulating wide temperature electrolyte by dissolving thermally stable lithium salts in low melting point and high boiling point solvents with low viscosity.^{7, 37-43} Herein, a dual-salt electrolyte of 0.6 M LiTFSI + 0.4 M LiDFOB EC/PC/EMC (1:1:3, by volume) is developed for 5 Ah

NCM523/G pouch cell. Wherein, carbonate solvents possessing low melting point (PC, $T_m = -48.8^\circ\text{C}$; EMC, $T_m = -53^\circ\text{C}$) and high boiling point (EC, $T_b = 243^\circ\text{C}$; PC, $T_b = 242^\circ\text{C}$) are selected for formulating the wide temperature range electrolyte. In the 1st formation cycle at room temperature (RT), 5 Ah NCM523/G pouch cell with the dual-salt electrolyte demonstrated high initial Coulombic efficiency of 85.8% (5.14/5.99 Ah) than that (47.6%, 2.18/4.58 Ah) of the pouch cell with 1 M LiPF₆ EC/PC/EMC (1:1:3, by volume) (Fig. 1a). Moreover, severe gas swelling of pouch cell with 1 M LiPF₆ EC/PC/EMC is observed (**Left inset in Fig. 1a**), due to the PC-induced formation of unstable solid-electrolyte-interphase (SEI) layer on graphite anode.⁴⁴⁻⁴⁵ As a sharp contrast, pouch cell with the dual-salt electrolyte shows no obvious swelling (**Right inset in Fig. 1a**), benefiting from the formation of stable SEI layer by LiDFOB salt.⁴⁶⁻⁴⁷ Therefore, 5 Ah NCM523/G pouch cell with the dual-salt electrolyte is employed for the following electrochemical and thermal safety study.

After the vacuum degassing procedure of formation process, the determined gravimetric energy density of 5 Ah NCM523/G pouch cell with dual-salt electrolyte is highly up to 208.8 Wh kg⁻¹. At RT at 0.5 C rate for 400 cycles, the pouch cell presents a high average Coulombic efficiency of 99.88% and delivers a discharge capacity retention of 92.72%, 84.10%, 74.90% and 68.77%, at the 100th, 200th, 300th, and 400th cycle, respectively (Fig. 1b-c). When the temperature is increased up to 60 °C, the discharge capacity retention of the pouch cell at 0.2 C rate is 82.23%, 79.02%, 76.56% and 74.48% at the 100th, 200th, 300th and 400th cycle, respectively, with an average Coulombic efficiency reaching to 99.92% (Fig. 1d-e). In subsequent, subzero temperature performance is revealed by discharging the room-temperature fully charged 5 Ah NCM523/G pouch cell, at varied subzero temperatures of -10 °C, -20 °C, -30 °C, and -40 °C, respectively (Fig. 1f). The corresponding discharge capacity retention is 85.79%,

75.76%, 64.46%, and 40.81%. In general, the high-energy 5 Ah NCM523/G pouch cell using the formulated dual-salt electrolyte is very competent for wide temperature range applications. Moreover, it is noted that, to the best of our knowledge,²⁹ this is the first case to evaluate the application of dual-salt electrolytes in LIBs over a wide temperature range, which is significant for the commercialization process of dual-salt electrolytes.

Heat generation during charge-discharge operation

Thermal anomalies inside the cell or pack in the absence of proper thermal management can instigate accelerated cell capacity degradation and even hazardous thermal runaway. Therefore, the heat generation accompanied with battery charge-discharge operation is receiving more and more attention. Generally, heat generated from battery cycling can be divided into reversible heat and irreversible heat. Irreversible heat refers to the ohmic heat from the polarization or overpotential of the cell, while reversible heat is determined by the measurement of cell entropic coefficient depending on the intrinsic nature of the electrode materials (relating with the atom arrangement in the crystal lattice).⁴⁸ Deciphering the heat generation law of a single cell is essential to design and optimize the battery thermal management system, which ensures batteries in a pack or module running in an ideal temperature range. Here, two boundary scenarios of adiabatic and isothermal environment, representing the worst and best case for the heat management, respectively, are considered for heat determination of the pouch cell with dual-salt electrolyte.

ARC (an adiabatic calorimeter) is a pivotal integrated technology to study the thermal safety of LIBs at multilevel, and research progress on ARC is reviewed by us very recently.²² In general, ARC will simulate an accurate adiabatic condition by keeping the cavity temperature consistent with the sample temperature, preventing the self-generated heat loss of sample. Therefore, ARC is the worse-case scenario. Here, the 5 Ah NCM523/G pouch cell with the dual-salt electrolyte is placed in the adiabatic cavity of ARC (BTC500, HEL, **Figure S1**) and connected with a charge/discharge apparatus. Obviously, the surface temperature of pouch cell increases during both charge and discharge process (Fig. 2a and **Figure S2a-c**). For example, at 0.5 C rate, the overall heat generation (19.5°C, 1.9 kJ) during the charge process is much higher than that (6.3°C, 0.6 kJ) of the discharge process. At varied C-rates, the self-heating rate curves during charge and discharge process are symmetrical (**Figure S2d-f**), evidencing that the heat generation mainly consisted of the irreversible joule heat and the reversible electrochemical reaction heat.^{49–50} Obviously, the reversible electrochemical reaction heat dominates the total heat at low rates and irreversible joule heat dominates the total heat at high rates. These results clearly tell us that, at the worst case of adiabatic condition, the 5 Ah NCM523/G pouch cell at higher rates will easily get thermal runaway in few cycles, revealing the importance of battery thermal management. As for the battery thermal management, it is necessary to determine the heat generation of a single cell at a constant temperature. Here, as a best-case scenario, IMC (isoBTC, HEL) is used to test the heat generation of the 5 Ah NCM523/G pouch cell at the isothermal condition (**Figure S3**). At 0.5 C rate at 30°C, the overall heat generation (1.2 kJ) during the charge process is much higher than that (0.4 kJ) of the discharge process (Fig. 2b). Clearly, the released energy during 1 charge-discharge cycle at isothermal

condition (1.6 kJ) is lower than that at the adiabatic condition (2.5 kJ). Interestingly, at 0.5 C rate, more heat is generated at both 10°C and 50°C when compared to 30°C, suggesting the importance of selecting work temperature for battery (**Figure S4**). The reversible and irreversible heat are determined based on the ohmic resistance and total heat generation.⁵¹ The internal resistance of the pouch cell is calculated by the hybrid pulse power characterization method (**Figure S5**). On the whole, the reversible heat dominates the total heat generation at 0.5 C rate, and the endothermic and exothermic reactions are distinguishable and transformable during the charge or discharge process (Fig. 2c). Compared to fresh pouch cell, long-term (400 cycles) cycled pouch cell demonstrates much higher heat release power at higher rates, especially at 1 C rate (Fig. 2d). In summary, the design of an efficient and smart battery thermal management system must comprehensively consider the effects of work temperature, state of charge (SOC), charge-discharge current rate, and charge-discharge protocol on heat generation, and IMC testing will give the answers.

Thermal runaway feature and mechanism

As a high-energy storage reservoir, LIBs easily get thermal runaway when operated under mechanical, electrical, and thermal abuse conditions. To develop an efficient battery safety risk controlling strategy, it is necessary to obtain some critical parameters, such as onset temperature for self-heating (T_{onset}), self-heating rate (SHR), thermal runaway temperature (T_{tr}), and maximum temperature (T_{max}), etc. Here, 5 Ah NCM523/G pouch cell using dual-salt electrolyte is placed in the cavity of ARC (BTC500, HEL, Fig. 3a and Figure S6), and the typical heat-wait-search (HWS) mode is used to study thermal runaway features of the pouch cell. Under the HWS mode of ARC, the built-in camera in cavity captures that smoke and flame is rapidly spurted out of the pouch cell (100% SOC, after the formation process) (Fig. 3b). Obviously, the T_{onset} , T_{tr} (SHR over $1^{\circ}\text{C min}^{-1}$ as the criteria) and T_{max} is determined to be 91°C, 171°C, and 516°C, respectively (Fig. 3c). After the thermal runaway process, the aluminum plastic film is severely damaged (inset in Fig. 3c). It is noted here, that most previous battery thermal runaway investigations focus on the fully charged cell (100% SOC) because of its violent thermal runaway hazardous, while the fact that fully discharged cell (0% SOC) also undergoes thermal runaway is neglected. Here, to explore the rooted mechanism for the triggering of thermal runaway behavior, 5 Ah NCM523/G pouch cell without dual-salt electrolyte and 5 Ah NCM523/G pouch cell with dual-salt electrolyte but without formation process are fabricated and tested by ARC under same conditions, and interestingly, both pouch cells do not present severe exothermic reactions related to the thermal runaway of pouch cell below 250°C (Fig. 3d). However, when the 5 Ah NCM523/G pouch cell with dual-salt electrolyte is cycled for one formation cycle (0% SOC), the thermal runaway occurs under the same testing condition in ARC ($T_{\text{onset}} = 141^{\circ}\text{C}$, $T_{\text{tr}} = 199^{\circ}\text{C}$, $T_{\text{max}} = 280^{\circ}\text{C}$). These results clearly tell us that the formed interfacial layer components between the electrolyte and electrodes play a crucial role in triggering the thermal runaway process of pouch cell. Therefore, we confirm that pouch cell after formation process will go thermal runaway anyway regardless of the SOC, and pouch cell with higher SOC demonstrates faster and more severe thermal runaway process (**Figure S7**).

To decipher the rooted mechanism for triggering the thermal runaway of NCM523/G pouch cell, ARC (BTC130, HEL) equipped with a small bomb chamber is used to study the thermal compatibility of battery components (Fig. 4a and Figure S8). In the Ar-filled glove box, the anode and cathode are carefully and separately disassembled from fully charged (100% SOC) and fully discharged (0% SOC) 5 Ah NCM523/G pouch cell. The as-formulated fresh dual-salt electrolyte presents a high T_{onset} of 218°C, suggesting its high thermal stability (Fig. 4b). The fully delithiated cathode/electrolyte (100% SOC) and lithiated cathode/electrolyte (0% SOC) demonstrate T_{onset} of 134°C (Fig. 4c) and 171°C (Fig. 4d), respectively. And the fully lithiated anode/electrolyte (100% SOC) and delithiated anode/electrolyte (0% SOC) exhibit the T_{onset} of 95°C (Fig. 4e) and 128°C (Fig. 4f), respectively. These results reveal that, at different SOCs, cathode/electrolyte and anode/electrolyte will inevitably go thermal runaway and anode/electrolyte is easier to get thermal runaway than cathode/electrolyte. In addition, higher thermal reactivity is presented at higher SOCs. Therefore, it is concluded here that high SOC is just the accelerating factor of battery thermal runaway, but not the root cause for triggering it. After thermal runaway of the dual-salt electrolyte, anode/electrolyte, and cathode/electrolyte, the remained incondensable gas species in the sealed bomb chamber is collected and analyzed by the mass spectrometer (MS), respectively (**Insets in Fig. 4b-e**). Wherein, the remained gas species for thermal runaway of sole as-formulated dual-salt electrolyte is mainly consisted of CO_2 (51.8%) and CH_4 (24.7%) (**Insets in Fig. 4b**). For fully delithiated NCM523 cathode/electrolyte (100% SOC), O_2 (87.9%) dominates the collected gas species after thermal runaway (**Insets in Fig. 4c**). Revealed by temperature-resolved XRD equipped with an *in-situ* heating module, when the temperature exceeds 200°C, the fully delithiated NCM523 cathode will release O_2 by phase transformation of layered structure ($(003)_{\text{R}}$) to spinel structure ($(111)_{\text{S}}$) and disordered spinel structure ($(108)_{\text{R}}$ and $(110)_{\text{R}}$) to the NiO-like rock-salt structure ($(440)_{\text{S}}$) (Fig. 4g). As an interest comparison, lithiated NCM523 cathode (0% SOC) reacting with electrolyte produces main gas species of CO_2 (48.7%), CH_4 (26.8%) and O_2 (13.4%). The dramatic decrease of O_2 percentage is possibly attributed to the well-preserved crystal structure of lithiated NCM523 cathode (0% SOC) (Fig. 4h). To further verify this, XRD patterns of the powders collected after thermal runaway of 0 and 100% SOC 5 Ah NCM523/G pouch cell are tested. It is presented that the fully delithiated NCM523 cathode (100% SOC) undergoes phase transformation and crystal structure collapse while the main layered structure of lithiated NCM523 cathode (0% SOC) is preserved (**Figure S9**). These results indicate that O_2 releasing accompanying with phase transformation of delithiated NCM523 cathode at high temperature around 200°C may aggravate the burning or explosion, but is not the rooted mechanism for triggering thermal runaway. Obviously, the rooted factor for triggering the thermal runaway still depend on anode side. After thermal runaway of fully lithiated anode/electrolyte (100% SOC), the dominated gas species is H_2 (68.2%), while CO_2 (39%), CH_4 (26.5%) and H_2 (18.8%) are the main gases determined for thermal runaway of unlithiated anode/electrolyte (0% SOC). Except the evolution of CO_2 and CH_4 from thermal decomposition of electrolyte, H_2 gas constitutes the most dominating gas species in the thermal runaway of anode/electrolyte at 0% and 100% SOC. This implies that, clarifying the origin of H_2 evolution is of great significance to understand the rooted triggering factor for thermal runaway. Temperature-resolved XRD

equipped with an *in-situ* heating module is also utilized to analyze the bulk phase change of graphite anode at different SOC. For lithiated graphite anode (100% SOC), the exothermic phase transformation of LiC_6 (001) to LiC_{12} (002), and LiC_{12} (002) to C (002) occurs at *ca.* 100°C and *ca.* 200°C, respectively (Fig. 4i). But, even if there is no such exothermic phase transformations for delithiated graphite anode (0% SOC) (Fig. 4i), the delithiated graphite anode/electrolyte (0% SOC) still exhibits thermal runaway and the self-heating happens earlier than lithiated NCM523 cathode/electrolyte (0% SOC). Hence, the LiC_6 - LiC_{12} -graphite phase transformation is also excluded to be the rooted factor for triggering thermal runaway. In subsequent, it is not difficult to infer that the thermal runaway of pouch cell is induced by the exothermic reactions related to the broken of the formed SEI layer on graphite anode. This is also evidenced by the fact that, cycled graphite anode (delithiated state, 0% SOC) reacting with electrolyte shows exothermic peak at *ca.* 80 ~ 170°C, which is not appeared for the uncycled pristine graphite anode and electrolyte, during the DSC test (**Figure S10**). Conventionally, SEI layer on graphite anode are typically determined to be consisted of inorganic species (such as LiF , Li_2CO_3 , Li_2O , Li_2C_2 , $\text{Li}_2\text{C}_2\text{O}_4$, LiOH , *etc.*) and organic species (such as ROCO_2Li , $(\text{CH}_2\text{OCO}_2\text{Li})_2$, ROLi , CH_3Li , *etc.*).⁵²⁻⁵⁷ Although the broken of SEI layer is always identified as the initial stage during the thermal runaway process, but the exothermic reactions related to the thermal decomposition of listed inorganic and organic species are not presented in detail to date. Moreover, the underlying cause for large amounts of H_2 evolution at graphite anode side is still remained unclear. Therefore, some unknown species must be still unidentified in the SEI layer of graphite anode. In some reports, it is suggested that the graphite anode surface is enriched of hydrogen,^{26, 58-59} but no further detailed evidence is provided. Herein, by employing a delicately-designed deuterium-oxide (D_2O) titration device connecting with an *on-line* gas analysis mass spectrometry (MS) system (Fig. 5a), we unprecedentedly identify the existence of H^- containing species on the surface of the graphite anode. Fully-lithiated graphite (100% SOC) and fully-delithiated graphite (0% SOC) is titrated by deuterium-oxide (D_2O) with the following guideline reactions: $\text{Li}_x\text{C}_6 + x\text{D}_2\text{O} \rightarrow x\text{LiOD} + \text{C}_6 + x/2 \text{D}_2\uparrow$, ($x \leq 1$); $\text{H}^- + \text{D}_2\text{O} \rightarrow \text{OD}^- + \text{HD}\uparrow$. Surprisingly, HD ($m/z = 3$) signal is observed for both fully-lithiated graphite (100% SOC) and fully-delithiated graphite (0% SOC). In addition, the mole of HD and D_2 ($m/z = 4$) at fully-lithiated graphite (100% SOC) is $0.14 \mu\text{mol mg}^{-1}$ and $4.26 \mu\text{mol mg}^{-1}$, respectively (Fig. 5b), which decrease to $0.014 \mu\text{mol mg}^{-1}$ and $0.029 \mu\text{mol mg}^{-1}$, respectively, when the graphite anode is fully-delithiated (0% SOC) (Fig. 5c). It is, the first time, discovered that H^- containing species, most probably in the form of LiH , do exist in the SEI layer of graphite anode, and the H^- containing species exhibit highly electrochemical reversibility at graphite anode surface during cycling. In another delicately-designed experiment, fully-lithiated graphite (100% SOC) is heated at 90°C, in the titration vessel of abovementioned *on-line* gas analysis mass spectrometry (MS) system. H_2 signal ($m/z = 2$) is detected after

heating to 90°C, confirming that the broken of SEI layer is accompanied by evolution of H_2 (**Figure S11**). Obviously, the released amount of H_2 (Fig. 4e-f) is highly correlated with the determined amount of H^- containing species. Highly lithiated graphite (high SOC) contains more H^- containing species and releases more H_2 when heating. Moreover, it is previously proposed that the recombination of the active

hydrogen to form H_2 will lead to huge generation of heat, which is even larger than that of H_2 burning in oxygen,²⁶ implying that the H^- -induced H_2 evolution accompanies with large amounts of heat releasing. Furthermore, the presence of H^- is also confirmed in graphite anode disassembled from NCM523/G and NCM811/G pouch cells (using conventional $LiPF_6$ based carbonate electrolyte), regardless of SOC, indicating this phenomenon is universal applicable for varied NCM/G cells (**Figure S12**). These amazing results indicate that the H^- induced H_2 releasing at the graphite anode side may be the rooted thermal runaway trigger of NCM523/G pouch cell, while the phase transformation of lithiated graphite anode and the O_2 -releasing by delithiated NCM cathode are just accelerating factors for thermal runaway.

The aforementioned released gases and temperature profiles during thermal runaway of anode/electrolyte and cathode/electrolyte are separately determined and analyzed, not considering of anode/cathode crosstalk. However, in practical cases, despite anode and cathode is physically separated by the separator, the porosity of separator always allow the crosstalk of byproducts.^{10, 60} Then the question comes: during the triggering process of thermal runaway, is there any crosstalk effect when the released gas species migrate through porous separators? To answer this question, a self-made two bomb chamber testing system is delicately fabricated, where the anode and cathode is placed separately, but the released gas species can flow freely by the connected pipeline, and two bomb chambers are heated by one same heating wire in the quasi-adiabatic cavity of ARC (**Figure S13**, and insets in Fig. 6a-b). Connected with the bomb with fully delithiated NCM523 cathode/electrolyte, the fully-lithiated graphite/electrolyte reaction delivers a same T_{onset} of $95^\circ C$ and a lower T_{tr} (from $306^\circ C$ to $247^\circ C$) (Fig. 6a), compared to the one bomb test of the fully-lithiated graphite/electrolyte mentioned above (Fig. 4e). This clearly tell us that the triggering of anode/electrolyte thermal runaway at low temperatures is not affected by gas species generated by cathode/electrolyte reactions. But at high temperatures, the released gas species (especially O_2) will accelerate the thermal runaway of anode/electrolyte. Another two-bomb testing reveals that the gas species (especially H_2) produced by anode/electrolyte decrease the thermal stability of cathode/electrolyte (Fig. 6b). In specific, T_{onset} drops from $136^\circ C$ to $116^\circ C$, and a sharp temperature rise from $159^\circ C$ to $285^\circ C$ is appeared in the HWS curve. Furthermore, gas species collected from the two-bomb system (100% SOC electrodes) are mainly consisted of CO_2 (28.5%), CH_4 (32.7%), H_2 (15.2%), and O_2 (12%), suggesting that H_2 from anode and O_2 from cathode side is consumed, and subsequently, evidencing the occurrence of the crosstalk of the released gas species during thermal runaway (**Figure S14**). Moreover, H_2 is preliminarily calculated to have higher affinity to NCM (**Figure S15**), suggesting that the released H_2 has high tendency to react with the NCM in elevated temperatures. In summary, it is concluded here that the H^- -induced H_2 releasing at anode side and H_2 migration to cathode side is the rooted thermal runaway trigger of NCM523/G pouch cell, while the phase transformation of lithiated graphite anode and the O_2 -releasing by delithiated NCM523 cathode are just accelerating factors for thermal runaway. Based on all the analysis and experiments, a modified and upgraded thermal runaway route map for 100% SOC NCM523/graphite pouch cell is depicted here (Fig. 6c): 1) under abuse (mechanical, electrical, or thermal) conditions, when the battery temperature

increases to *ca.* 100°C, mild exothermic reactions related to phase transformation of LiC₆ to LiC₁₂ and SEI layer destruction happens; The SEI layer broken is accompanied by H⁻-induced H₂ releasing and corresponding large amounts of heat releasing; 2) Parts of released H₂ will diffuse to cathode side, possibly reacting with the fully delithiated NCM to release heat; The reactions in step 1 and step 2 will raise the temperature to *ca.* 200°C, at which the polyolefin separators have been melted and partial short circuit between the cathode and anode poles will continue to push up the temperature; 3) when the temperature is pushed up to the range of 200–250°C, three severe exothermic reactions happens (electrolyte decomposition; phase transformation of LiC₁₂ to graphite; and O₂-releasing by delithiated NCM523 cathode) and the released large amounts of gases (O₂, H₂, CH₄, CO, C₂H₄, etc.) lead to the final severe thermal runaway (smoke, fire, and even explosion).

Conclusion

In this paper, a LiTFSI-LiDFOB based dual-salt electrolyte has been successfully and unprecedentedly demonstrated to possess high compatibility with a high-energy (208.8 Wh kg⁻¹) 5 Ah NCM523/G pouch cell. This pouch cell delivers excellent electrochemical performances over a wide temperature range (-40 ~ 60°C). In subsequent, the thermal safety characteristics of this high-energy pouch cell is investigated. Heat determination under adiabatic condition states the necessity of designing battery thermal management system, while heat determination under isothermal condition reveals that an efficient and smart battery thermal management system must comprehensively consider the effects of work temperature, state of charge (SOC), charge-discharge current rate, and charge-discharge protocol on heat generation. More importantly, by varied advanced characterization techniques, it is innovatively proposed that the H⁻-induced H₂ releasing at anode side and H₂ migration to cathode side is the rooted thermal runaway trigger of NCM523/G pouch cell, while the phase transformation of lithiated graphite anode and the O₂-releasing by delithiated NCM523 cathode are just accelerating factors for thermal runaway. These findings will shed promising lights on thermal runaway prevention as well as development of high energy safe LIBs.

Experimental Procedures

Pouch cell and electrolyte

Dry (no electrolyte injection) 5 Ah LiNi_{0.5}Co_{0.2}Mn_{0.3}O₂/graphite (NCM523/G) pouch cells with gas pocket were manufactured by Shandong Kingpin Energy Co., Ltd., China. All battery grade lithium salts (LiPF₆, LiDFOB, and LiTFSI) and solvents (EC, PC, and EMC) were purchased without purification (Suzhou Qianmin Chemistry Co., Ltd., China). The dual-salt electrolyte was formulated by dissolving 0.6 M LiTFSI and 0.4 M LiDFOB in carbonate solvents of EC/PC/EMC (1:1:3, by volume), and 0.05 M LiPF₆ was used as functional additive. For comparison, 1.0 M LiPF₆ EC/PC/EMC (1:1:3, by volume) was also prepared. All electrolytes were prepared in an argon-filled glovebox (Mikrouna, China) with H₂O and O₂ less than 1 ppm.

Electrochemical measurements over wide temperature range

The 5 Ah NCM/G pouch cells were charged and discharged using a LAND battery testing system (Wuhan LAND electronics Co., Ltd. China). All pouch cells were charged and discharged at 0.1 C at room temperature for the one formation cycle, then vacuum degassed to remove gas pocket. For room temperature cycling performance at 0.5 C, all pouch cells were charged to 4.2 V, followed by a constant potential step at 4.2 V for 10 min, then discharged to 3.0 V. For 60°C cycling performance at 0.2 C, all pouch cells were charged to 4.2 V, followed by a constant potential step at 4.2 V for 10 min, then discharged to 3.0 V. For low temperature discharge performance, all pouch cells were charged to 4.2 V at 0.2 C, followed by a constant potential step at 4.2 V for 10 min, then discharged to 3.0 V at 0.1 C at varied subzero temperatures of -10 °C, -20 °C, -30 °C, and -40 °C.

Heat generation at adiabatic condition

For heat generation determination at adiabatic condition, the 5 Ah NCM/G pouch cells were put inside the ARC cavity (BTC500, HEL, England) and connected with a charge-discharge device (Wuhan LAND electronics Co., Ltd. China) (See **Figure S1**). The adiabatic test mode of ARC is used, and three different current rate of 0.25 C, 0.5 C, and 1 C were used to investigate the temperature increase and self-heating rate of the pouch cell during the charge and discharge process. After each charge or discharge process, the cavity temperature of ARC was cooled back to the initial temperature of 30°C.

Heat generation at isothermal condition

Isothermal heat generation during charge and discharge process was determined by an isothermal battery calorimeter (IBC, iso-BTC, HEL, England). The tested pouch cell was enclosed by graphite film with high heat conductivity. Heating sheets were fixed on graphite film (fixed on the side close to pouch cell), and power sensor was fixed on pouch cell (See **Figure S3**). The pouch cell was tested at 0.5 C at varied temperatures of 10 °C, 30 °C, and 50 °C, respectively, and the corresponding total specific heat generation rate (q) was determined.

The total specific heat generation rate (q) included the reversible heat generation rate (q_r) and irreversible heat generation (q_i). q was determined by the IBC testing, and q_i is calculated by I^2R , where I is the working current, and R is the total internal resistance. The reversible heat generation rate (q_r) was obtained by $q_r = q - q_i$. The total internal resistance R of the pouch cell was determined by the hybrid pulse power characterization using the battery test system. The pouch cell was adjusted to a specific SOC (10%, 20%, 30%, 40%, 50%, 60%, 70%, 80%, 90%, and 100%), and then the following protocol was used: 1 C rate pulse for 10 s discharge, followed with a 40 s rest, then a 0.75 C pulse was used to charge for 10 s. Each SOC adjustment was followed by a one-hour rest period. Finally, the total internal resistance R during charge and discharge was calculated as mentioned previously.⁵¹

Study of thermal runaway feature and mechanism

Thermal runaway study of 5 Ah NCM/G pouch cell was conducted using an ARC BTC500 (HEL, England), which was equipped with a digital camera (see **Figure S6**). Here, typical Heat-Wait-Seek (HWS) mode was adopted for testing: one heating step was 5 °C; detection limit was 0.03 °C min⁻¹; the temperature was raised from 40 to 250 °C. The thermal runaway criteria was 1 °C min⁻¹.

Thermal compatibility study of battery materials was investigated by a small standard ARC (BTC130, HEL, England, see Fig. 4a and **Figure S8**). The anode and cathode are carefully disassembled from fully charged (100% SOC) and fully discharged (0% SOC) 5 Ah NCM523/G pouch cells, in an argon-filled glovebox. The electrode materials were carefully removed from the current collector with a surgical blade. 0.5 mL electrolyte and 1 g electrode material were transferred into the small bomb chamber made of Hastelloy alloy. Here, typical HWS mode was adopted for testing: one heating step was 5 °C; detection limit was 0.03 °C min⁻¹; the temperature was raised from 40 to 250 °C. The thermal runaway criteria was 1 °C min⁻¹. When the small bomb chamber was cooled down after thermal runaway, the released gases was collected to be analyzed by a mass spectrum (MS, HPR-20, Hiden Analytical Ltd.).

The thermal stability of battery materials was also tested in a Simultaneous Thermal Analyzer (STA, Netzsch): heating rate was 5 °C min⁻¹; the temperature was raised from 25 to 500 °C. Temperature-resolved X-ray diffraction XRD (with Cu K α radiation, $\lambda = 1.5406 \text{ \AA}$) was tested on a Ultima IV of Rigaku: the sample was sealed in an Ar-filled container; the angle ranged from 10° to 80° with a scan speed of 20° min⁻¹; the temperature was raised from 30 °C to 400 °C with a heating rate of 1 °C min⁻¹.

Graphite anode with 0% SOC and 100% SOC was well-sealed in a container of the titration unit, respectively. After connecting the sample-containing titration unit to the *on-line* gas analysis system, the Ar carrier gas was switched to go through the titration unit, then 1 ml D₂O was injected and the gas species (mainly D₂ and HD) was recorded by the (MS HPR-20, Hiden Analytical Ltd.). In another test, the unit containing the 100% SOC graphite anode was heated to 90 °C, and the released gas species were detected (See **Figure S11a**).

To study the crosstalk effects of released gas species, a self-made two bomb chamber testing system is delicately fabricated (**Figure S13**), where the anode and cathode is placed separately, but the released gas species can flow freely by the connected pipeline, and two bomb chambers are heated by one same heating wire in the quasi-adiabatic cavity of ARC.

Declarations

ACKNOWLEDGMENTS

This original research was supported by the National Key R&D Program of China (Grant No. 2017YFE0127600), the Strategic Priority Research Program of Chinese Academy of Sciences (Grant No. XDA22010603), the National Natural Science Foundation of China (No. U1706229, 51625204 and 52037006).

AUTHOR CONTRIBUTIONS

L. H. and G. X. contributed equally to this work. G. C. proposed the topic of the manuscript. L. H., J. L., B., X., D. L., H. L. and M. Z. conducted the experiments, X. D. conducted the calculations, L. H. and G. X. wrote the manuscript, P. H., G. C., and L. C. revised the manuscript.

DECLARATION OF INTERESTS

The authors declare no competing interests.

References

1. Goodenough, J. B., (2015). Energy storage materials: a perspective. *Energy Storage Mater.* 1, 158–161.
2. Goodenough, J. B.; Kim, Y., (2010). Challenges for rechargeable Li batteries. *Chem. mater.* 22 (3), 587–603.
3. Xu, G.; Han, P.; Dong, S.; Liu, H.; Cui, G.; Chen, L., (2017). Li₄Ti₅O₁₂-based energy conversion and storage systems: Status and prospects. *Coord. Chem. Rev.* 343, 139–184.
4. Liu, K.; Liu, Y.; Lin, D.; Pei, A.; Cui, Y., (2018) Materials for lithium-ion battery safety. *Sci. adv.* 4 (6), eaas9820.
5. Larsson, F.; Andersson, P.; Mellander, B.-E., (2016). Lithium-ion battery aspects on fires in electrified vehicles on the basis of experimental abuse tests. *Batteries* 2 (2), 9.
6. Loveridge, M. J.; Remy, G.; Kourra, N.; Genieser, R.; Barai, A.; Lain, M. J.; Guo, Y.; Amor-Segan, M.; Williams, M. A.; Amietszajew, T., (2018). Looking deeper into the Galaxy (Note 7). *Batteries* 4 (1), 3.
7. Rodrigues, M.-T. F.; Babu, G.; Gullapalli, H.; Kalaga, K.; Sayed, F. N.; Kato, K.; Joyner, J.; Ajayan, P. M., (2017). A materials perspective on Li-ion batteries at extreme temperatures. *Nat. Energy* 2 (8), 1–14.
8. Li, Y.; Feng, X.; Ren, D.; Ouyang, M.; Lu, L.; Han, X., (2019). Thermal Runaway Triggered by Plated Lithium on the Anode after Fast Charging. *ACS Appl. Mater. Inter.* 11 (50), 46839–46850.
9. Geng, Z.; Lu, J.; Li, Q.; Qiu, J.; Wang, Y.; Peng, J.; Huang, J.; Li, W.; Yu, X.; Li, H., (2019). Lithium metal batteries capable of stable operation at elevated temperature. *Energy Storage Mater.* 23, 646–652.
10. Liu, X.; Ren, D.; Hsu, H.; Feng, X.; Xu, G.-L.; Zhuang, M.; Gao, H.; Lu, L.; Han, X.; Chu, Z., (2018). Thermal runaway of lithium-ion batteries without internal short circuit. *Joule* 2 (10), 2047–2064.
11. Huang, Q.; Ma, L.; Liu, A.; Ma, X.; Li, J.; Wang, J.; Dahn, J., (2018). The reactivity of charged positive Li_{1-n} [Ni_xMn_yCo_z] O₂ electrodes with electrolyte at elevated temperatures using accelerating rate calorimetry. *J. Power Sources* 390, 78–86.

12. Zhou, Q.; Dong, S.; Lv, Z.; Xu, G.; Huang, L.; Wang, Q.; Cui, Z.; Cui, G., (2020). A Temperature-Responsive Electrolyte Endowing Superior Safety Characteristic of Lithium Metal Batteries. *Adv. Energy Mater.* 10 (6), 1903441.
13. Profatilova, I. A.; Langer, T.; Badillo, J. P.; Schmitz, A.; Orthner, H.; Wiggers, H.; Passerini, S.; Winter, M., (2012). Thermally induced reactions between lithiated nano-silicon electrode and electrolyte for lithium-ion batteries. *J. Electrochem. Soc.* 159 (5), A657.
14. Mukai, K.; Inoue, T.; Hasegawa, M., (2017). Rationalizing thermal reactions of C6Lix negative electrode with nonaqueous electrolyte. *J. Power Sources* 366, 185–192.
15. Francis, C.; Louey, R.; Sammut, K.; Best, A. S., (2018). Thermal stability of pyrrolidinium-FSI ionic liquid electrolyte and lithium-ion electrodes at elevated temperatures. *J. Electrochem. Soc.* 165 (7), A1204.
16. Ping, P.; Wang, Q.; Huang, P.; Sun, J.; Chen, C., (2014). Thermal behaviour analysis of lithium-ion battery at elevated temperature using deconvolution method. *Appl. Energy* 129, 261–273.
17. Holzapfel, M.; Alloin, F.; Yazami, R., (2002). Microcalorimetric study of the reactivity of lithiated HOPG with organic electrolytes. *J. Phys. Chem. B* 106 (51), 13165–13175.
18. Downie, L.; Dahn, J., (2014). Determination of the voltage dependence of parasitic heat flow in lithium ion cells using isothermal microcalorimetry. *J. Electrochem. Soc.* 161 (12), A1782-A1787.
19. Lu, W.; Prakash, J., (2003). In situ measurements of heat generation in a Li/mesocarbon microbead half-cell. *J. Electrochem. Soc.* 150 (3), A262-A266.
20. Glazier, S.; Li, J.; Louli, A.; Allen, J.; Dahn, J., (2017). An analysis of artificial and natural graphite in lithium ion pouch cells using ultra-high precision coulometry, isothermal microcalorimetry, gas evolution, long term cycling and pressure measurements. *J. Electrochem. Soc.* 164 (14), A3545-A3555.
21. Wang, Q.; Jiang, L.; Yu, Y.; Sun, J., (2019). Progress of enhancing the safety of lithium ion battery from the electrolyte aspect. *Nano Energy* 55, 93–114.
22. Xu, G.; Huang, L.; Lu, C.; Zhou, X.; Cui, G., (2020). Revealing the multilevel thermal safety of lithium batteries. *Energy Storage Mater.* 31, 72–86
23. Hou, J.; Lu, L.; Wang, L.; Ohma, A.; Ren, D.; Feng, X.; Li, Y.; Li, Y.; Ootani, I.; Han, X., (2020). Thermal runaway of Lithium-ion batteries employing LiN(SO₂F)₂-based concentrated electrolytes. *Nat. Commun.* 11 (1), 1–11.
24. Feng, X.; Ren, D.; He, X.; Ouyang, M., (2020). Mitigating Thermal Runaway of Lithium-Ion Batteries. *Joule* 4, 1–28.
25. Lyu, P.; Liu, X.; Qu, J.; Zhao, J.; Huo, Y.; Qu, Z.; Rao, Z., (2020). Recent advances of thermal safety of lithium ion battery for energy storage. *Energy Storage Mater.* 31. 195–220.
26. Galushkin, N.; Yazvinskaya, N.; Galushkin, D., (2018). Mechanism of thermal runaway in lithium-ion cells. *J. Electrochem. Soc.* 165 (7), A1303.

27. Parekh, M. H.; Sediako, A. D.; Naseri, A.; Thomson, M. J.; Pol, V. G., (2020). In Situ Mechanistic Elucidation of Superior Si-C-Graphite Li-Ion Battery Anode Formation with Thermal Safety Aspects. *Adv. Energy Mater.* 10 (2), 1902799.
28. Feng, X.; Ouyang, M.; Liu, X.; Lu, L.; Xia, Y.; He, X., (2018). Thermal runaway mechanism of lithium ion battery for electric vehicles: A review. *Energy Storage Mater.* 10, 246–267.
29. Xu, G.; Shangguan, X.; Dong, S.; Zhou, X.; Cui, G., (2020) Formulation of Blended-Lithium-Salt Electrolytes for Lithium Batteries. *Angew. Chem. Int. Ed.* 59 (9), 3400–3415.
30. Campion, C. L.; Li, W.; Lucht, B. L., (2005). Thermal decomposition of LiPF₆-based electrolytes for lithium-ion batteries. *J. Electrochem. Soc.* 152 (12), A2327-A2334.
31. Xu, G.; Liu, Z.; Zhang, C.; Cui, G.; Chen, L., (2015). Strategies for improving the cyclability and thermostability of LiMn₂O₄-based batteries at elevated temperatures. *J. Mater. Chem. A* 3 (8), 4092–4123.
32. Liu, Z.; Chai, J.; Xu, G.; Wang, Q.; Cui, G., (2015). Functional lithium borate salts and their potential application in high performance lithium batteries. *Coord. Chem. Rev.* 292, 56–73.
33. Haregewoin, A. M.; Wotango, A. S.; Hwang, B.-J., (2016). Electrolyte additives for lithium ion battery electrodes: progress and perspectives. *Energy Environ. Sci.* 9 (6), 1955–1988.
34. Han, J.-G.; Lee, J. B.; Cha, A.; Lee, T. K.; Cho, W.; Chae, S.; Kang, S. J.; Kwak, S. K.; Cho, J.; Hong, S. Y., (2018). Unsymmetrical fluorinated malonateborate as an amphoteric additive for high-energy-density lithium-ion batteries. *Energy Environ. Sci.* 11 (6), 1552–1562.
35. Li, Y.; Wan, S.; Veith, G. M.; Unocic, R. R.; Paranthaman, M. P.; Dai, S.; Sun, X. G., (2017). A Novel Electrolyte Salt Additive for Lithium-Ion Batteries with Voltages Greater than 4.7 V. *Adv. Energy Mater.* 7 (4), 1601397.
36. Lu, D.; Xu, G.; Hu, Z.; Cui, Z.; Wang, X.; Li, J.; Huang, L.; Du, X.; Wang, Y.; Ma, J., (2019). Deciphering the Interface of a High-Voltage (5 V-Class) Li-Ion Battery Containing Additive-Assisted Sulfolane-Based Electrolyte. *Small Methods* 3 (10), 1900546.
37. Xu, G.; Huang, S.; Cui, Z.; Du, X.; Wang, X.; Lu, D.; Shangguan, X.; Ma, J.; Han, P.; Zhou, X., (2019). Functional additives assisted ester-carbonate electrolyte enables wide temperature operation of a high-voltage (5 V-Class) Li-ion battery. *J. Power Sources* 416, 29–36.
38. Shangguan, X.; Xu, G.; Cui, Z.; Wang, Q.; Du, X.; Chen, K.; Huang, S.; Jia, G.; Li, F.; Wang, X., (2019). Additive-Assisted Novel Dual-Salt Electrolyte Addresses Wide Temperature Operation of Lithium–Metal Batteries. *Small* 15 (16), 1900269.
39. Fan, X.; Ji, X.; Chen, L.; Chen, J.; Deng, T.; Han, F.; Yue, J.; Piao, N.; Wang, R.; Zhou, X., (2019). All-temperature batteries enabled by fluorinated electrolytes with non-polar solvents. *Nat. Energy* 4 (10), 882–890.
40. Hou, J.; Yang, M.; Wang, D.; Zhang, J., (2020). Lithium-Ion Batteries: Fundamentals and Challenges of Lithium Ion Batteries at Temperatures between – 40 and 60° C. *Adv. Energy Mater.* 10 (18), 2070079.
41. Zhu, G.; Wen, K.; Lv, W.; Zhou, X.; Liang, Y.; Yang, F.; Chen, Z.; Zou, M.; Li, J.; Zhang, Y., (2015). Materials insights into low-temperature performances of lithium-ion batteries. *J. Power Sources* 300, 29–40.

42. Li, Q.; Jiao, S.; Luo, L.; Ding, M. S.; Zheng, J.; Cartmell, S. S.; Wang, C.-M.; Xu, K.; Zhang, J.-G.; Xu, W., (2017). Wide-temperature electrolytes for lithium-ion batteries. *ACS Appl. Mater. Inter.* 9 (22), 18826–18835.
43. Xu, K., (2004). Nonaqueous liquid electrolytes for lithium-based rechargeable batteries. *Chem. rev.* 104 (10), 4303–4418.
44. Xu, K., (2009). Whether EC and PC differ in interphasial chemistry on graphitic anode and how. *J. Electrochem.Soc.* 156 (9), A751.
45. Ming, J.; Cao, Z.; Wu, Y.; Wahyudi, W.; Wang, W.; Guo, X.; Cavallo, L.; Hwang, J.-Y.; Shamim, A.; Li, L.-J., (2019). New insight on the role of electrolyte additives in rechargeable lithium ion batteries. *ACS Energy Lett.* 4 (11), 2613–2622.
46. Zhang, S. S., (2006). An unique lithium salt for the improved electrolyte of Li-ion battery. *Electrochem. Commun.* 8 (9), 1423–1428.
47. Zhang, S. S., (2007). Electrochemical study of the formation of a solid electrolyte interface on graphite in a LiBC₂O₄F₂-based electrolyte. *J. power sources* 163 (2), 713–718.
48. Manikandan, B.; Yap, C.; Balaya, P., (2017). Towards understanding heat generation characteristics of Li-Ion batteries by calorimetry, impedance, and potentiometry studies. *J. Electrochem.Soc.* 164 (12), A2794-A2800.
49. Gunnarshaug, A. F.; Kjelstrup, S.; Bedeaux, D.; Richter, F.; Burheim, O. S., (2020). The reversible heat effects at lithium iron phosphate-and graphite electrodes. *Electrochem. Acta* 337, 135567.
50. Liu, G.; Ouyang, M.; Lu, L.; Li, J.; Han, X., (2014). Analysis of the heat generation of lithium-ion battery during charging and discharging considering different influencing factors. *J. Therm. Anal. Calorim.* 116 (2), 1001–1010.
51. Wang, K.; Gao, F.; Zhu, Y.; Liu, H.; Qi, C.; Yang, K.; Jiao, Q., (2018). Internal resistance and heat generation of soft package Li₄Ti₅O₁₂ battery during charge and discharge. *Energy* 149, 364–374.
52. Verma, P.; Maire, P.; Novák, P., (2010). A review of the features and analyses of the solid electrolyte interphase in Li-ion batteries. *Electrochim. Acta* 55(22), 6332–6341.
53. Xu, K., (2014). Electrolytes and interphases in Li-ion batteries and beyond. *Chem. rev.* 114 (23), 11503–11618.
54. Gauthier, M.; Carney, T. J.; Grimaud, A.; Giordano, L.; Pour, N.; Chang, H.-H.; Fenning, D. P.; Lux, S. F.; Paschos, O.; Bauer, C., (2015). Electrode–electrolyte interface in Li-ion batteries: current understanding and new insights. *J. Phys. Chem. Lett.* 6 (22), 4653–4672.
55. Fang, C.; Li, J.; Zhang, M.; Zhang, Y.; Yang, F.; Lee, J. Z.; Lee, M.-H.; Alvarado, J.; Schroeder, M. A.; Yang, Y., (2019). Quantifying inactive lithium in lithium metal batteries. *Nature* 572 (7770), 511–515.
56. Yu, X.; Manthiram, A., (2018). Electrode–electrolyte interfaces in lithium-based batteries. *Energy Environ. Sci.* 11 (3), 527–543.
57. Bridges, C. A.; Sun, X.-G.; Zhao, J.; Paranthaman, M. P.; Dai, S., (2012). In situ observation of solid electrolyte interphase formation in ordered mesoporous hard carbon by small-angle neutron

scattering. J. Phys. Chem. C 116 (14), 7701–7711.

58. Omichi, K.; Ramos-Sanchez, G.; Rao, R.; Pierce, N.; Chen, G.; Balbuena, P.; Harutyunyan, A., (2015). Origin of excess irreversible capacity in lithium-ion batteries based on carbon nanostructures. J. Electrochem.Soc. 162 (10), A2106.
59. Zheng, X.; Yang, C.; Chang, X.; Wang, T.; Ye, M.; Lu, J.; Zhou, H.; Zheng, J.; Li, X., (2018). Synergism of Rare Earth Trihydrides and Graphite in Lithium Storage: Evidence of Hydrogen-Enhanced Lithiation. Adv. Mater. 30 (3), 1704353.
60. Metzger, M.; Strehle, B.; Solchenbach, S.; Gasteiger, H. A., (2016). Origin of H₂ evolution in LIBs: H₂O reduction vs. electrolyte oxidation. J. Electrochem.Soc.163 (5), A798.

Figures

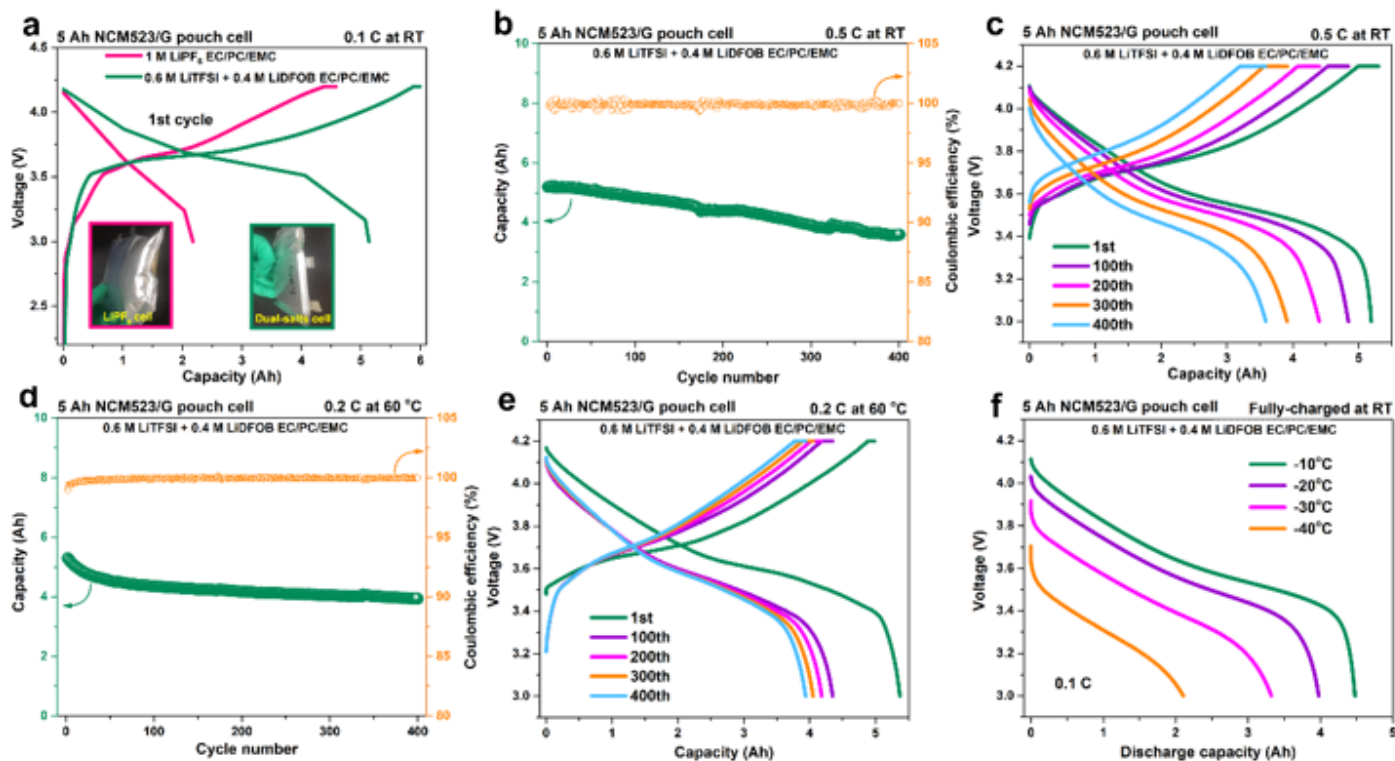


Figure 1

(a) The 1st formation cycle of 5 Ah NCM523/G pouch cell using 1 M LiPF₆ EC/PC/EMC and a dual-salt electrolyte of 0.6 M LiTFSI + 0.4 M LiDFOB EC/PC/EMC. The electrochemical cycling performances of 5 Ah NCM523/G pouch cell using the dual-salt electrolyte, (b)(c) at room temperature (RT) and (d)(e) at 60°C, respectively. (f) The low temperature discharge curves of 5 Ah NCM523/G pouch cell using the dual-salt electrolyte. Insets in (a) are the photographs of pouch cells after the formation process.

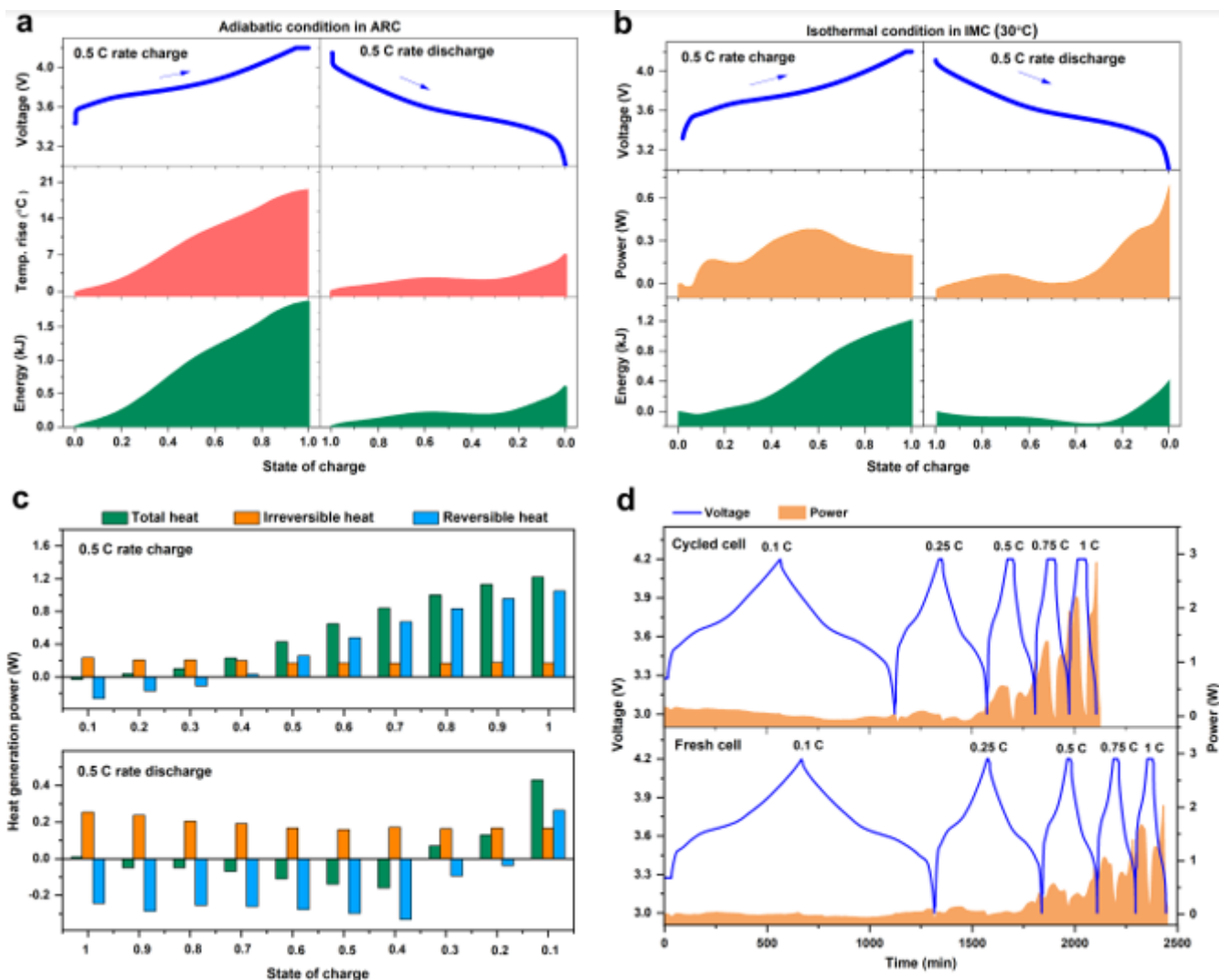


Figure 2

(a) The voltage curve, temperature rise and released energy when charging and discharging 5 Ah NCM523/G pouch cell at 0.5 C rate under the adiabatic mode of ARC equipment (initial temperature 30°C). (b) The voltage curve, heat release power and released energy when charging and discharging 5 Ah NCM523/G pouch cell at 0.5 C rate at 30°C under isothermal condition of IMC equipment. (c) The determined total heat generation power, reversible heat generation power and irreversible heat generation power when charging and discharging 5 Ah NCM523/G pouch cell at 0.5 C rate. (d) The heat generation power of fresh cell and cycled (400 cycles) cell at varied C-rates.

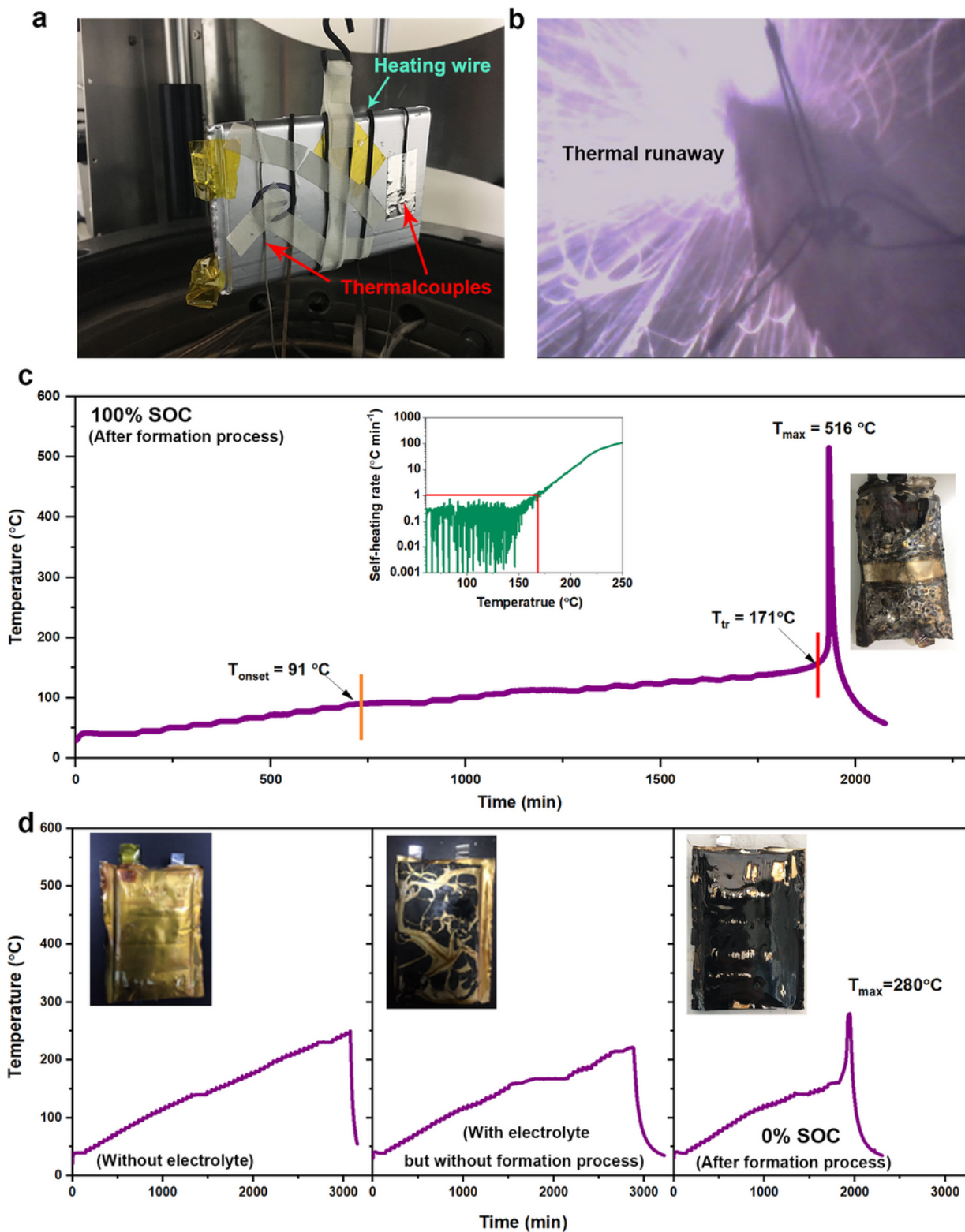


Figure 3

(a) The photograph of 5 Ah NCM523/G pouch cell in ARC (BTC500, HEL) for thermal runaway study. (b) The captured photograph when 5 Ah NCM523/G pouch cell gets thermal runaway in ARC. (c) Temperature profile when 5 Ah NCM523/G pouch cell (100% SOC, after formation process) is tested by the heat-wait-search (HWS) mode of ARC. Insets of (c) are the corresponding self-heating rate curve and the wreck of tested pouch cell. (d) Temperature profiles when varied types of 5 Ah NCM523/G pouch cell

is tested by the heat-wait-search (HWS) mode of ARC. Insets of (d) are the corresponding wrecks of tested pouch cells.

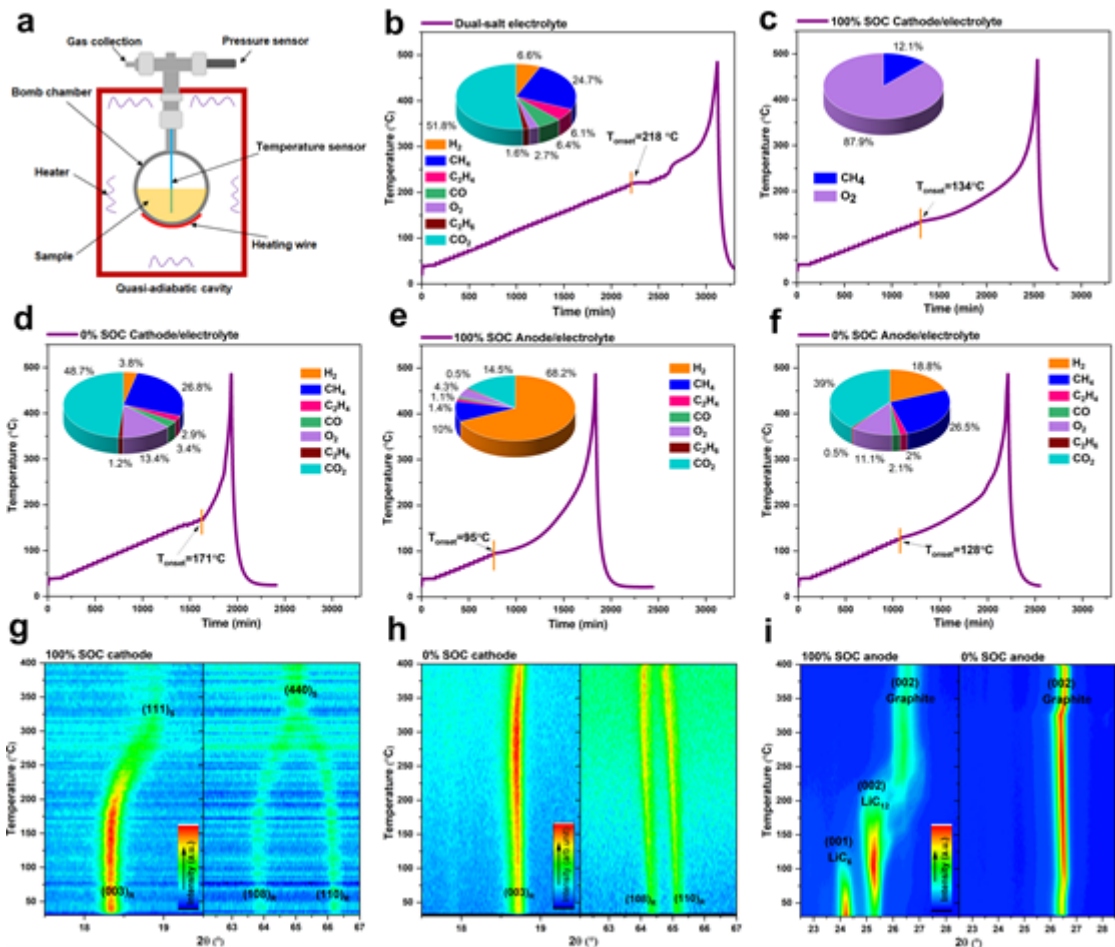


Figure 4

(a) Schematic illustration of the working principle of ARC (BTC130, HEL) with a small bomb chamber. Temperature profiles when (b) dual-salt electrolyte, (c) 100% SOC cathode/electrolyte, (d) 0% SOC cathode/electrolyte, (g) 100% SOC anode/electrolyte, and (h) 0% SOC anode/electrolyte, are tested by the heat-wait-search (HWS) mode of ARC. The insets in (b)(c)(d)(g)(h) are the determined components percentage in collected gas after ARC testing. XRD patterns of (e), (f) cathode and (i) anode by increasing the temperature from 30 to 400°C. The anode and cathode are carefully and separately dissembled from fully charged (100% SOC) and fully discharged (0% SOC) 5 Ah NCM523/G pouch cells.

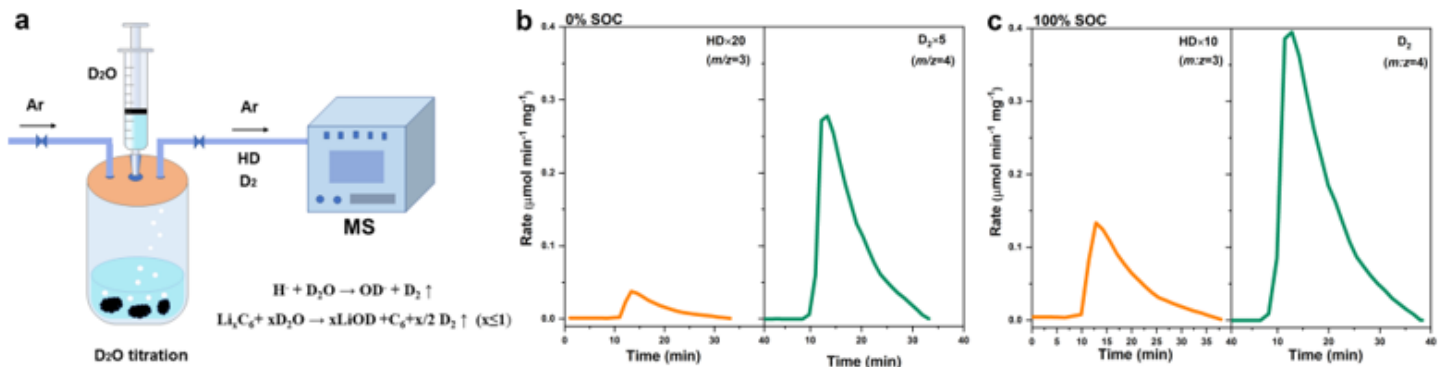


Figure 5

(a) Schematic illustration of delicately-designed on-line D2O titration gas analysis MS system. The HD and D2 evolution rate curve after D2O titration on samples of (b) fully-delithiated graphite (0% SOC) and (c) fully-lithiated graphite (100% SOC) . (mg-1, divided by the sample mass for titration). The graphite anodes are carefully and separately dissembled from fully charged (100% SOC) and fully discharged (0% SOC) 5 Ah NCM523/G pouch cells.

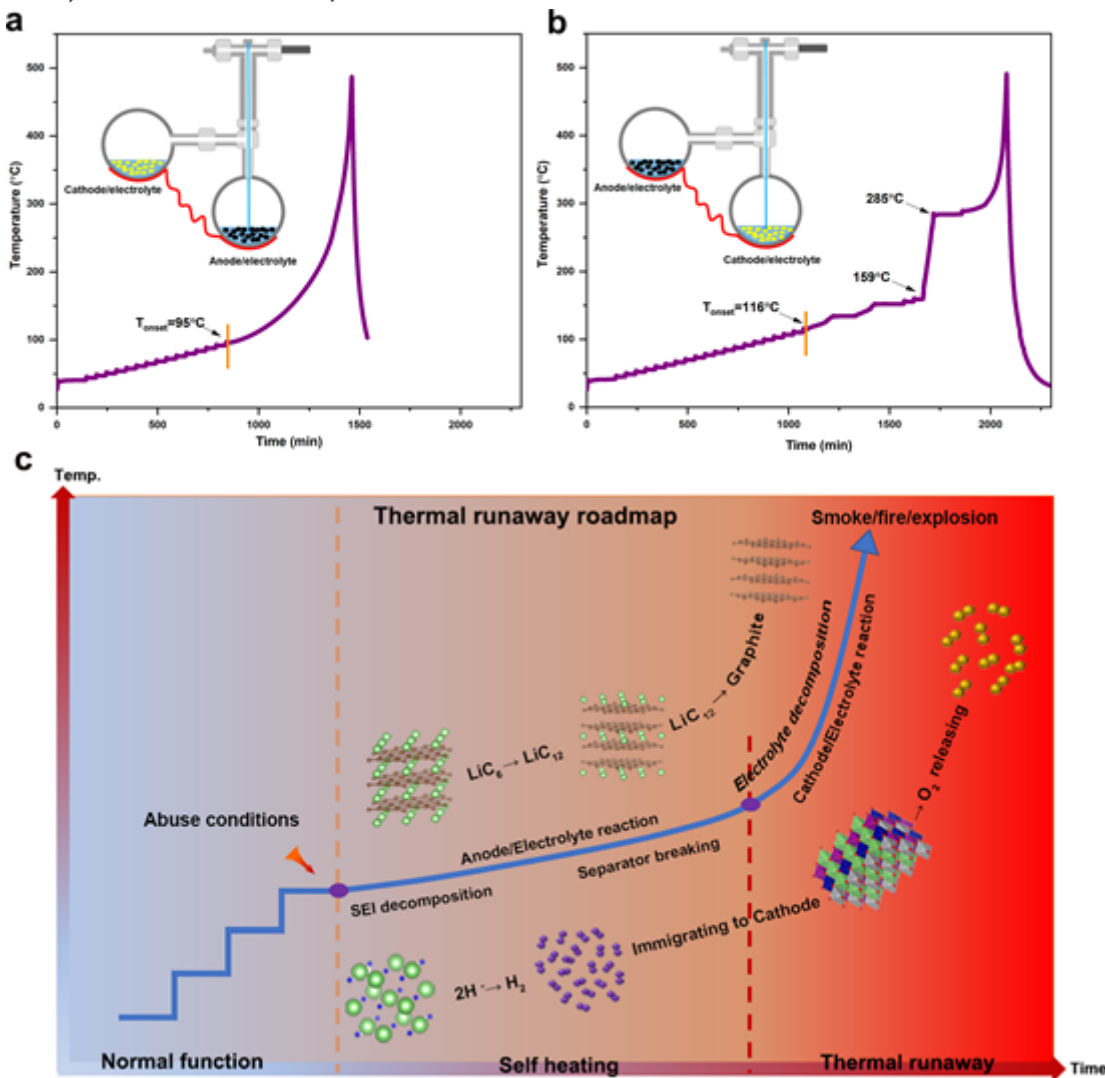


Figure 6

(a) Temperature profile when 100% SOC anode/electrolyte (connected with a bomb chamber containing 100% SOC cathode/electrolyte) are tested by the heat-wait-search (HWS) mode of ARC. (b) Temperature profile when 100% SOC cathode/electrolyte (connected with a bomb chamber containing 100% SOC anode/electrolyte) are tested by the heat-wait-search (HWS) mode of ARC. Insets are the specific settings. (c) Thermal runaway route map for fully charged NCM/graphite cell.

Supplementary Files

This is a list of supplementary files associated with this preprint. Click to download.

- [SupportingInformation.docx](#)